Article

Characterization of Raindrop Size Distribution over Santa Clara Valley

Nathan Quinn [1] and Sen Chiao [2],*

1   Center for Applied Atmospheric Research and Education, San Jose State University, San Jose, CA 95192, USA; nathan.quinn@sjsu.edu
2   NOAA Cooperative Science Center in Atmospheric Sciences and Meteorology, Howard University, Washington, DC 20059, USA
*   Correspondence: sen.chiao@howard.edu

Abstract: This study presents a year-long (January 2019–April 2020) analysis of the Z–R relationship and drop size distribution (DSD) scaling parameters for size, concentration, and shape of rain events over Santa Clara Valley, CA. External influences were analyzed based on synoptic variability and seasons. For the former, 850 hPa winds were separated into groups based on direction and magnitude. Results show that greater drop size, lower concentration, and larger shape parameters for spring, while winter and fall showed smaller drop sizes, higher concentrations, and smaller shape parameters. For synoptic variability, southeasterly-to-southwesterly flow was associated with larger drop sizes, larger concentrations, and smaller shape parameters relative to northwesterly flow. Differences in the DSD scaling parameter values and Z–R relationship were also observed between strong and weak low-level flow. The results of this study suggest that it is beneficial to derive specific microphysical relationships based on seasons and different synoptic events to improve radar rain rate retrieval algorithms using the Z–R relationship.

Keywords: precipitation; Z–R relationship; disdrometer; microphysics; drop size distribution

1. Introduction

The San Francisco Bay area receives most of its precipitation via atmospheric rivers (ARs) and mid-latitude frontal systems during the wet season (i.e., October to March). The synoptic-scale dynamics associated with ARs and mid-latitude frontal systems are well-established. However, previous research shows that complex terrain, such as the Santa Cruz Mountains, can enhance orographic lift and significantly alter precipitation processes [1], complicating the accuracy and precision of numerical weather prediction (NWP) forecast models and radar-based quantitative precipitation estimation (RQPE) via local S-band radar. For instance, the Santa Clara Valley Water District (SCVWD) in San Jose, CA, utilizes quantitative precipitation forecasts (QPFs) for their hydrologic models; however, their accuracy and precision depends on the initial inputs from mesoscale weather models, which can have ample amounts of uncertainty due to the rain shadow effect (Behringer 2019) [1]. NWP forecast models are highly dependent on the accuracy of rainfall distribution over time and space [2]. Understanding the characteristics of precipitation, such as the drop size distribution (DSD), is a principal factor for the improvement of NWP forecast models and RQPE. Marshall and Palmer (1948) [3] compared DSD and radar echoes and found a relationship between precipitation intensity and reflectivity in association with the drop size distribution through the power law equation, which is the relationship between the radar reflectivity factor (Z) and the rain rate (R).

$$Z = aR^b \tag{1}$$

$$R = \frac{6\pi}{10^4} \int_0^\infty N(D)\, v(D)\, D^3\, dD \tag{2}$$

$$Z = \int_0^\infty N(D)\, D^6 dD \tag{3}$$

where rain rate (R) in Equation (2) represents the number of rain drops per unit of volume and diameter interval N(D) ($mm^{-1} \cdot m^{-3}$) and the terminal fall velocity of a rain drop of a specific diameter v(D) ($m \cdot s^{-1}$). The prefactor (a) and exponent (b) surrounding the rain rate (R) in Equation (1) are influenced by the characteristics of Equations (2) and (3), such as drop size and concentration. The concentration (N(D)) in Equation (4) is described as the concentration of DSD depending on the slope parameter (N_0 ($m^{-3} \cdot mm^{-1}$)) and the size parameter (Λ (mm^{-1})).

$$N(D) = N_0 \exp(-\Lambda D) \tag{4}$$

Marshall and Palmer (1948) [3] were unable to capture the instantaneous rain rate DSD using Equation (4). Therefore, the gamma distribution method (n(D)) was proposed by Ulbrich et al. (1983) [4], as shown in Equation (5).

$$n(D) = N_0 D^\mu \exp(-\Lambda D) \tag{5}$$

The gamma distribution method depends upon three parameters (N_0, μ, Δ) in Equation (5), which are defined as the concentration, shape, and size, respectively. These parameters are useful for identifying a broader range of DSD with respect to the Marshal–Palmer two-parameter exponential distribution (N(D)) in Equation (4), which is obtained by setting the shape parameter to zero.

Characteristics of raindrop sizes, seasons, synoptic conditions, hydrology, and geography influence the prefactor (a) and exponent (b) in the Z–R relationship (Wu et al., 2018) [5]. The varying nature of reflectivity (Z) and the components of the gamma distribution method (n(D)) over time and space can be used as a tool to identify patterns and characteristics of the drop size spectra associated with external factors [6–8]. Wen et al. [6] found that the largest drop sizes and greatest concentrations occurred during summer, whereas winter provided the lowest concentration values in eastern China due to the "maritime" nature of convective processes, which influenced the region throughout the year. In Cévennes-Vivarais, [7] found that the summer season provided the largest drop diameters and lowest concentrations, whereas winter is associated with smaller drop diameters and the highest concentrations. This study revealed unique Z–R relationships that supported larger prefactors and smaller exponents in relation to larger diameters and lower concentrations. Furthermore, S. Hachani et al. (2017) [7] observed that synoptic events in the Cévennes-Vivarais region associated with southwesterly flow produced lower drop concentrations and larger drop diameters, whereas synoptic events that were characterized by Atlantic flow produced the least variability of DSD and were associated with larger concentrations and smaller drop sizes. In Cazadero, CA, a study by Martner et al. [8] revealed that during non-convective periods associated with a strong El Nino winter, the melting layer radar bright band was completely absent, which suggests greater concentrations of small drops and lower concentrations of large drops.

In San Jose, CA, precipitation coming out of the west must reach the lee side of the Santa Cruz Mountains. However, precipitation reaching the ground is uncertain due to the rain shadow effect. This causes specific rain microphysical processes to occur that are highly dependent upon dynamic configurations and the barrier shape [9–13]. Previous research showed that weaker rain shadows on the eastern slope of the Washington Cascades were associated with prefrontal (warm frontal) periods of a passing mid-latitude frontal system [9,10]. Additionally, Mass et al. (2015) [9] suggested that weak rain shadow events were modulated by southeasterly upslope flow due to mid-latitude frontal systems

approaching the Washington Cascades, whereas Purnell et al. (2018) [11] found that the strongest rain shadows over the Olympic Mountains were due to mountain wave descent on the lee side. In addition to dynamical influences, the shape of the barrier is an important factor that partially modulates strong and weak rain shadows. For instance, stationary air on the lee side of a dome-shaped mountain is more easily diminished by adjacent low-level airflow around the barrier [12,13].

Due to the microphysical characteristics of precipitation intensity varying with seasons, synoptic configurations, and geography over time and space, the fixed Z–R relationship may not be accurate for rainfall events of different intensities. To counteract these erroneous predictions, multiple Z–R relationships are used in the NEXRAD (Next-Generation Radar) network. Some of these Z–R relationships include the non-tropical convective ($Z = 300R^{1.4}$), stratiform/orographic ($Z = 200R^{1.6}$), and cool season ($Z = 75R^{2.0}$). Surface disdrometer measurements offer a careful examination of unique microphysical relationships associated with differing rain events. The goal of this study is to identify precipitation distribution patterns in association with seasonal and synoptic variability in San Jose, CA. Sections 2–5 focus on Data and Methods, Results, Discussion, and Conclusions and future work, respectively.

2. Data and Methods

2.1. Data, Quality Control, and Limitations

Disdrometer data can be accessed through the SJSU Center for Applied Atmospheric Research and Education (CAARE) [14]. This study includes data from one OTT Parsivel laser-based optical disdrometer located at the top of Duncan Hall (159 feet) at San Jose State University (37.34° N, 121.88° W). An OTT Parsivel disdrometer measures precipitation as a mathematical integration of droplets passing through a cross section (54 cm^2) in each sample time. For this study, a sample time of 5 min was used to allocate enough drops for each time step. When a drop passes through the volume, the reference signal abates and is proportional to the difference between the area of the section line of the drop and the area of the section line of the volume it passes through [15]. The velocity is determined based on instants in time of entrance and exit of the volume [16]. The measuring ranges for the particle size of liquid precipitation, solid precipitation, and particle speed are 0.20 mm to 8 mm, 0.2 mm to 25 mm, and 0.20 m·s^{-1} to 20 m·s^{-1}, respectively. Each range of sizes is divided into a 32 by 32 array that allows us to allocate parameters of interest.

For this study, the measurements included rain events between 16 January 2019 and 6 April 2020. To reduce noise within the data, a quality control (QC) methodology was adopted, which included:

1. Incorporation of rain rates greater than 0.5 mm·h^{-1} for the Z–R relationship [17];
2. Allocation of drops between 0.2 mm and 7 mm. This methodology disregards drops that are too small or too large [18].

The limited sampling area for this disdrometer acts to reduce multiple drops passing through the area. However, multiple drops can pass through, especially if the concentration is high, resulting in large drops that have unrealistic fall velocities. Additionally, drops that splash on the head of the sensor can cause non-realistic drops that are particularly small [19]. For this study, there were three instances of drop sizes that had unrealistic fall velocities, occurring on 16 January 2019, 27 November 2019, and 5 April 2020. After filtering out the non-realistic data, five minute time steps were generated.

2.2. DSD Parameters

The number of raindrops per unit of volume and diameter interval (N(D)) is represented by Equation (6), where a multitude of integral parameters are calculated based on the moments of order (k) of the DSD (M_k).

$$M_k = \int_0^\infty N(D) \, D^k dD \tag{6}$$

A normalized DSD (N(D)) in Equation (7) was introduced by J. Testud et al. (2001) [20] to avoid dependency of the concentration upon the shape parameter (μ). The concentration (N_0^*) represents the new scaling parameter now being independent of the shape parameter (μ).

$$N(D) = N_0^* \; D^\mu \; \frac{\Gamma(4)(4+\mu)^{4+\mu}}{4^4 \, \Gamma(4+\mu)} \left(\frac{D}{D_m} \right) \exp \left[\left(-\frac{(4+\mu)}{D_m} D \right) \right] \tag{7}$$

$$D_m = \frac{M_4}{M_3} \tag{8}$$

Three parameters are necessary to determine the normalized gamma DSD in Equation (5). The mean volume diameter (D_m) is based on the two moments shown in Equation (8), while the concentration parameter (N_0^*) is based on the two moments shown in Equation (9) [20]. Lastly, the shape parameter (μ) is based on the three moments in time shown in Equation (10). The method used to calculate the shape parameter (μ) was proposed by V.N. Bring, V. Chandrasekar. 2001 [21], representing a minimization of the MSE (mean squared error) of the gamma DSD.

$$N_0^* = \frac{4^4}{\Gamma(4)} \frac{M_3^5}{M_4^4} = N_0 D_m^\mu \frac{\Gamma(4+\mu)}{\Gamma(4)} \frac{4^4}{(4+\mu)^{4+\mu}} \tag{9}$$

$$\mu = \frac{3M_4 M_3 - 4M_3^2}{M_3^2 - M_4 M_2} \tag{10}$$

For this study, the concentration (N_w) is indicated by Equation (11). (ρ_W) is the water density in g cm^{-3}, and (W) is the rainwater content in g m^{-3}. Equation (11) can be interpreted as the intercept parameter of an exponential DSD (N_0) with the same liquid water content (LWC) and mean drop size (D_m) as the actual DSD [22]. D_0 is defined as the median volume diameter and is related to the shape parameter (μ) by Equation (12).

$$N_w = \frac{4^4}{\pi \rho_w} \left(\frac{10^3 \, W}{D_m^4} \right) \tag{11}$$

$$\frac{D_0}{D_m} = \frac{3.67 + \mu}{4 + \mu} \tag{12}$$

The gamma distribution DSD (n(D)) is achieved within a limited range of minimum drop size (D_{min}) to a maximum drop size (D_{max}). D_{min} is set to 0, and the resulting gamma distribution (n(D)) is shown in Equation (13). The methods used to calculate the gamma distribution DSD parameters were developed by V.N. Bring, V. Chandrasekar. 2001 [21]. The software used to calculate the DSD parameters was developed by Joseph Hardin et al. (2017) [23].

$$n(D) = N_0 D^\mu \exp(-\Lambda D) \, (0 < D < D_{max}) \tag{13}$$

2.3. Radar Parameters

To calculate the reflectivity in DBZ, the reflectivity factor (Z) and rain rate (R) in Equations (1) and (2) form a linear relationship, as shown in Equation (14). Reflectivity (DBZ) is expressed in decibels of (Z) and (R). The rain rate (R; in m·s^{-1}) is related to the statistical moment of raindrop size (D) described in Equation (2). In addition, the

differential reflectivity (Zdr) shown in Equation (15) is defined as the ratio of the horizontal attenuation to vertical attenuation. In this study, Equation (15) was used to understand the relationship between differential reflectivity (Zdr) and mean volume diameter (D_m). The methods used to calculate reflectivity (DBZ) in Equation (14) and differential reflectivity (Zdr) in Equation (15) were proposed by Beard et al., 1987 [24]. The software used to calculate radar parameters was developed by Joseph Hardin et al. (2017) [23].

$$DBZ = 10 \log(a) + bdBR \tag{14}$$

$$Zdr = \frac{Z_h}{Z_v} \tag{15}$$

2.4. External Factors

The DSD scaling parameters and the Z–R relationship were analyzed based on two factors that may be able to explain differences within the recorded data: (1) seasons and (2) direction and magnitude of 850 hPa winds.

2.4.1. Seasons

To study the influence of seasons on the DSD scaling parameters and the Z–R relationship, the disdrometer data were grouped at separate times of the year: January and February of 2019 were grouped and labeled as winter, March and April of 2020 were labeled as spring, and the end of November and December of 2019 were labeled as fall. A violin plot of the scaling parameters and a Z vs. R scatter plot with a line of best fit were used to visualize the data. The exponential power law fit was calculated based on Levenburg–Marquardt minimization [23].

2.4.2. Direction and Magnitude of Low-Level Flow (850 hPa Winds)

Global forecast system (GFS) 0.25 degree resolution model data at a six-hour temporal resolution in NETCDF format were used to classify each rain event [25]. A qualitative analysis was performed on 850 hPa winds occurring from January 2019 to April 2020. The classification is shown in Table 1.

Table 1. Categorization of the magnitude and direction of 850 hPa winds. The first two conditions represent low-level flow out of the southwest at different magnitudes, while the last two conditions represent low-level flow out of the northwest at different magnitudes.

Condition	Sustained Winds (Knots) @ 850 hPa	Direction
1	5–20	Southeast to southwest
2	30–65	Southeast to southwest
3	5–15	Northwest to southwest
4	15–30	Northwest to southwest

Condition 1 and condition 2 are represented by 850 hPa winds between 5 knots and 20 knots and between 30 knots and 65 knots, respectively. The 850 hPa wind direction for condition 1 and condition 2 was southeast and southwest and was associated with 850 hPa warm air advection (WAA). Using WPC's Surface Analysis Archive [26], condition 1 and condition 2 were found to be associated with the prefrontal or warm sectors of multiple mid-latitude frontal systems, which coincide with greater instances of WAA and southwest winds. A total of 858 five-minute rainy timesteps were generated, providing most of the rainy time steps relative to condition 3 and condition 4 (119 five-minute rainy timesteps). Condition 3 and condition 4 represented 850 hPa winds between 5 knots and 15 knots and between 15 knots and 30 knots, respectively. The direction of the winds was northwest to southwest and was associated with prominent 850 hPa cold air advection (CAA). Using

the WPC's Surface Analysis Archive [26], condition 3 and condition 4 were determined to belong to the post-frontal region of multiple mid-latitude frontal systems, contributing to the prominent CAA and northwesterly flow for condition 3 and condition 4.

2.5. Rain Types

To identify different rain types associated with the external factors, a set of reflectivity and rain rate conditions proposed by C. Caracciolo et al. [27] was used to divide the rain types for the mid-latitudes (Table 2).

Table 2. The set of conditions that describe the rain type for the mid-latitudes. S, stratiform; Heavy S, heavy stratiform; C, convection; Shallow C, shallow convection.

Classification	Condition
S	if $R < 10$ mm·h^{-1} and $Z < 38$ dBZ
Heavy S	if $R > 10$ mm·h^{-1} and $Z < 38$ dBZ
C	if $R \geq 10$ mm·h^{-1} and $Z \geq 38$ dBZ
Shallow C	if $R < 10$ mm·h^{-1} and $Z > 38$ dBZ

3. Results

3.1. External Factors

In this section, we delve into the influence of seasonal and synoptic variability on the DSD characteristics. For seasonal and synoptic variations, the analysis includes a Z vs. R scatter plot and a violin plot for the DSD scaling parameters. For synoptic variability, radar parameters and DSD scaling parameters are included. Each variable was statistically analyzed and is presented in the form of a table.

3.1.1. Seasonal Influence

Figures 1 and 2 show the seasonal influence on the Z–R relationship and DSD scaling parameters given by Equations (1) and (13). Notable differences in winter include greater concentration values (log N_w = 3.51 mm^{-3}· mm^{-1}), smaller drop size values (D_m = 1.06 mm), and lower shape parameter values (μ = 8.13) (Table 3). This explains the shift in the Z–R relationship, supporting lower (greater) reflectivity values for low to moderate (moderate to high) rain rates, in association with the lowest prefactor (186) and the greatest exponent (1.75) among all the seasons. Fall is characterized by smaller drop sizes (D_m = 1.05 mm), larger shape parameter (μ) values (10.02), and concentration (logN_w) values that between those of the spring and the fall (logN_w = 3.35 mm^{-3}· mm^{-1}). Additionally, drop sizes in the fall produced the smallest variability relative to the other seasons. The combination of these scaling parameter values explains the Z–R relationship, which favors the lowest reflectivity values for low to high rain rates and is associated with a prefactor (204) and exponent (1.61) between the winter and spring. Spring is represented by larger drop sizes (D_m = 1.15 mm), lower concentration (logN_w = 3.25 mm^{-3}· mm^{-1}) values, and shape parameter (μ) values between those of the fall and winter (μ = 9.16). The values obtained from the scaling parameters explains the results found in the Z–R relationship, which suggests greater reflectivity values for low to moderate rain rates and lower reflectivity values for higher rain rates. As a result, spring corresponds to the greatest prefactor (472) and the lowest exponent (1.37) among all seasons.
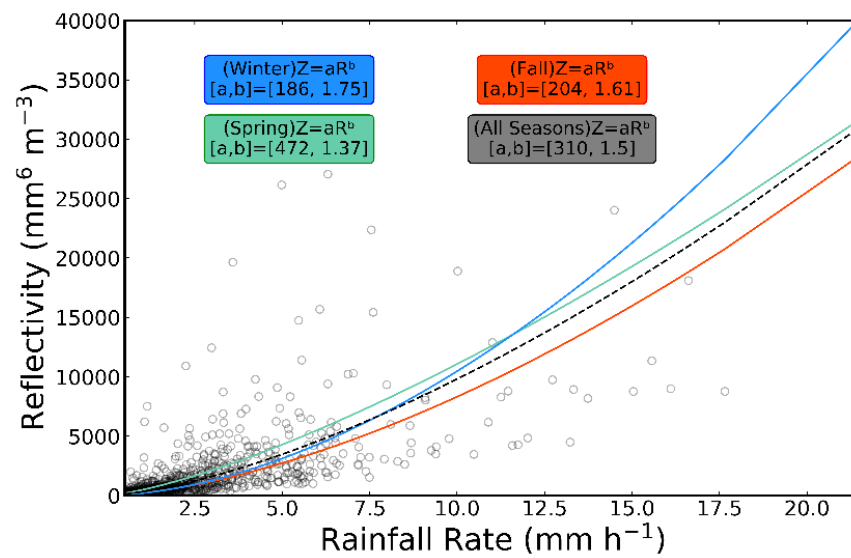
Figure 1. Influence of seasons on the Z–R relationship. Winter includes January and February of 2019, fall includes November and December of 2019, and spring includes March and April of 2020.
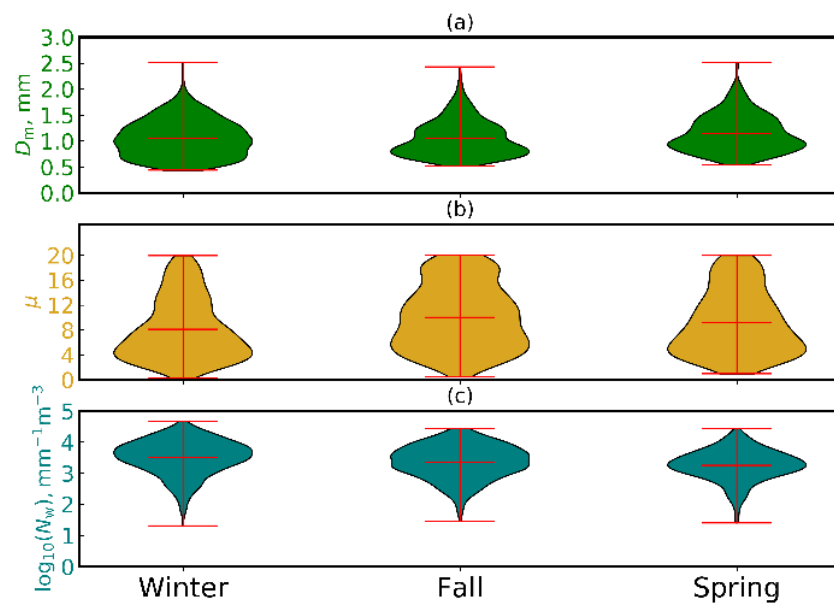

Figure 2. Seasonal influence on distributions of the DSD scaling parameters allocated during the winter, fall, and spring: (**a**) mean volume diameter; (**b**) shape; (**c**) concentration. Maximum, minimum, and average values are included.

Table 3. These statistics reflect the influence of seasons upon the scaling parameters. For winter, fall, and spring, the average (M), minimum (Min), maximum (Max), and standard deviation (SD) are shown.

	Winter					Fall					Spring			
	M	**Min**	**Max**	**SD**		**M**	**Min**	**Max**	**SD**		**M**	**Min**	**Max**	**SD**
D_m	1.06	0.44	2.51	0.36	D_m	1.05	0.51	2.43	0.34	D_m	1.15	0.54	2.52	0.35
μ	8.13	0.19	19.94	4.90	μ	10.0	1.24	19.98	5.11	μ	9.16	0.97	19.96	5.06
$\log N_w$	3.51	1.31	4.66	0.56	$\log N_w$	3.36	1.46	4.43	0.54	$\log N_w$	3.25	1.41	4.42	0.50

One peculiar finding that occurred was the concentration values between the winter and fall seasons; the drop sizes (D_m) were synonymous between the two seasons, but the concentration ($logN_w$) in fall was slightly lower than that in winter. As shown in Table 4, convective rain occurred 0.66 % of the time in winter and 1.44 % of the time in fall. Interestingly, spring is associated with the average largest drop sizes (D_m and D_0) and lowest average concentration ($logN_w$) values but accounts for a smaller percentage of convective rain (0.56%) and a larger percentage of stratiform rain (97.70%). Additionally, fewer heavy stratiform rain events occur in spring (0%) relative to fall and winter, and more shallow convective rain events (1.69%) occur in spring relative to fall (Table 4).

Table 4. Percentage of rainfall type by season. Four main types: stratiform, heavy stratiform, convective, and shallow convective.

Season	n	S (%)	Heavy S (%)	C (%)	Shallow C (%)
Winter	785	97.20	0.39	0.66	1.78
Fall	627	96.90	0.47	1.44	1.12
Spring	533	97.70	0.00	0.56	1.69

3.1.2. Direction of Low-Level Flow Influence

To gain an in-depth understanding of how low-level flow influences drop sizes over the study region, a select number of cases was chosen based on conditions described in Section 2.4.2. Figures 3 and 4 represent the influence of wind direction on the Z–R relationship and DSD scaling parameters. Southeast-to-southwest flow is characterized by greater concentration ($logN_w$) values, larger drop size (D_m) values, and smaller shape parameter (μ) values, on average (see Table 5). This explains the southeast-to-southwest Z–R relationship, which is associated with greater prefactor (297) and exponent (1.54) values and suggests larger reflectivity values for low to high rain rates. In contrast, northwest-to-southwest flow is characterized by smaller drop sizes (D_m), slightly higher concentrations ($logN_w$), and larger shape parameter values (μ). The resulting Z–R relationship reflects a lower prefactor (188) and lower exponent (1.40) and indicates lower reflectivity values for low to high rain rates.
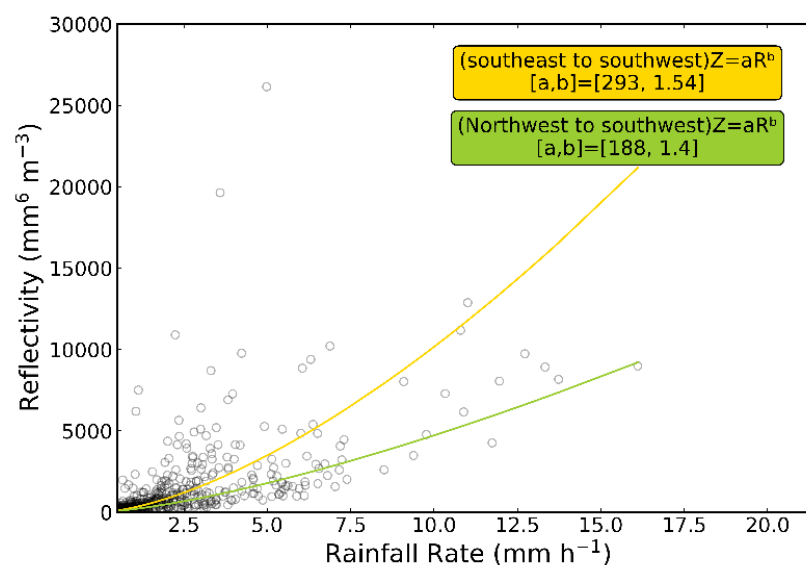

Figure 3. The influence of wind direction on the Z–R relationship. The yellow and green lines indicate the best fit for southwest and northwest flow, respectively.
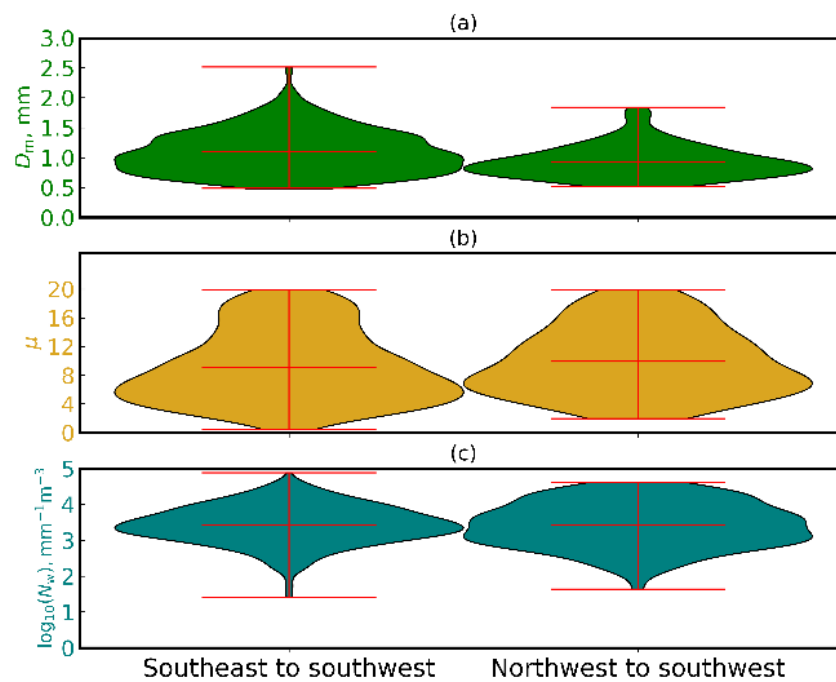
Figure 4. Influence of wind direction on the distributions of the DSD scaling parameters in the form of a violin plot: (**a**) mean mass diameter; (**b**) shape; (**c**) concentration.

Table 5. Mean (M), minimum (Min), maximum (Max), and standard deviation (SD) for the DSD scaling and radar parameters for southeast-to-southwest and northwest-to-southwest flow.

	Southeast-to-Southwest Flow					Northwest-to-Southwest Flow			
	M	Min	Max	SD		M	Min	Max	SD
$logN_w$	3.43	1.52	4.85	0.53	$logN_w$	3.42	1.64	4.61	0.62
D_m	0.99	0.484	2.52	0.36	D_m	0.93	0.52	1.84	0.27
μ	9.11	0.437	19.93	4.96	μ	9.33	1.96	19.85	4.63

Figure 5 shows the influence of wind direction on the following relationships: concentration vs. median volume drop size (Figure 5a,b), horizontal reflectivity vs. differential reflectivity (Figure 5c,d), and differential reflectivity vs. mean volume drop size (Figure 5e,f). On average, southeast-to-southwest flow is represented by larger drop sizes (D_0) and slightly lower concentration ($logN_w$) values, with more variability in drop size than concentration. This explains the shift in values illustrated in Figure 5b, which favors synonymous concentrations ($logN_w$) relative to northwest-to-southwest flow and larger drop sizes (D_0). In contrast, northwest-to-southwest flow is characterized by slightly higher concentrations ($logN_w$) and smaller drop sizes (D_0), which explains the shift towards smaller drop sizes (D_0) illustrated in Figure 5a. The red dashed line in Figure 5c,d indicates a C-band attenuation correction scheme proposed by V. N. Bringi et al. (2001) [28] and is accurate from 0 dBZ to 30 dBZ for northwest-to-southwest flow and southeast-to-southwest flow. As shown in Figure 5e, the maximum frequency of differential reflectivity (Zdr) values between 0 dB and 0.5 dB occurs in association with a drop size (D_m) of less than 1 mm, whereas Figure 5f shows relatively more occurrences of smaller differential reflectivity (Zdr) values and drop size (D_m) values. This is indicative of drops being more oblate and larger in association with southeast-to-southwest flow than northwest-to-southwest flow, as also influenced by the greater number of convective rain events (Tables 6 and 7).
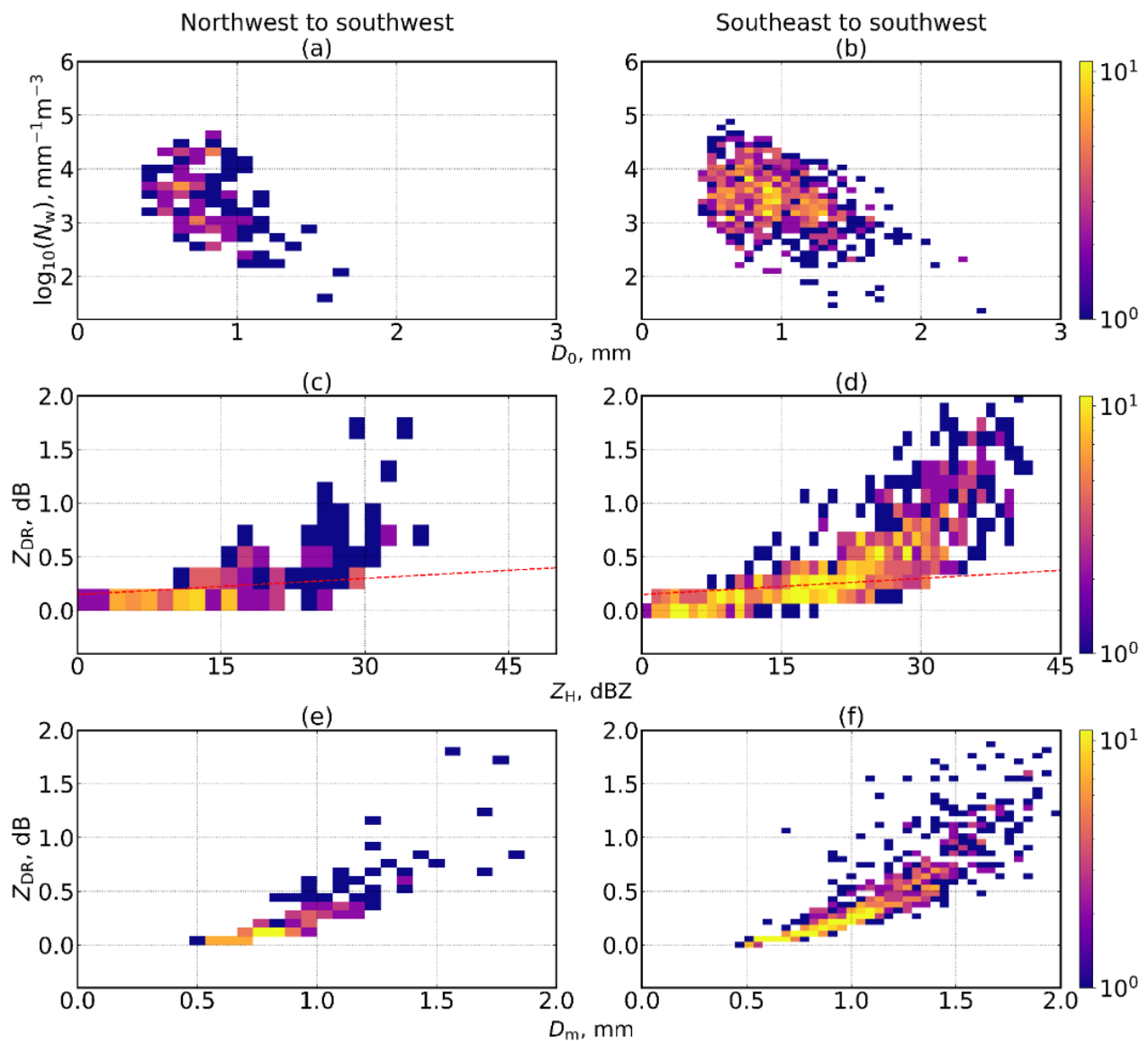
Figure 5. Series of two-dimensional histograms representing the influence of northwest-to-southwest flow and southeast-to-southwest flow on specific radar and DSD parameters: (**a**,**b**) D_0 vs. $\log N_w$ for northwest and southwest flow; (**c**,**d**) ZH vs. Zdr for northwest and southwest flow; (**e**,**f**) D_m vs. ZDR for northwest and southwest flow.

Table 6. Mean (M), minimum (Min), maximum (Max), and standard deviation (SD) for the DSD scaling parameters for southeast-to-southwest and northwest-to-southwest flow.

	Southeast-to-Southwest Flow					Northwest-to-Southwest Flow			
	M	**Min**	**Max**	**SD**		**M**	**Min**	**Max**	**SD**
D_0	0.95	0.41	2.41	0.31	D_0	0.81	0.44	1.64	0.23
$\log N_w$	3.43	1.52	4.85	0.53	$\log N_w$	3.42	1.64	4.61	0.62
ZH	21.28	0.59	44.17	9.77	ZH	16.39	0.71	35.08	8.45
ZDR	0.55	0.046	3.03	0.44	ZDR	0.29	0.026	1.78	0.31

Table 7. Percentage of rainfall type based on 850 hPa wind direction. n, number of rainy time steps (5 min); S, stratiform; Heavy S, heavy stratiform; C rain, convective rain; shallow C, shallow convective.

Condition	n	S (%)	Heavy S (%)	C Rain (%)	Shallow C (%)
Southwest	858	97.3	0.342	0.932	1.52
Northwest	119	100	0.00	0.00	0.00

3.1.3. Magnitude and Direction of Low-Level Flow Influence

Figures 6 and 7 show the influence of low-level flow at different magnitudes and directions on the Z–R relationship and the DSD scaling parameters. The directions can be broken down in to four subgroups: condition 1 and condition 2 (southeast-to-southwest flow) and condition 3 and condition 4 (northwest-to-southwest flow).

Southeast-to-southwest flow:

(1) Condition 1 is characterized by larger drop sizes (D_m), lower concentrations ($\log N_w$), and smaller shape parameter (μ) values relative to condition 2;
(2) Condition 2 is characterized by smaller drop sizes (D_m), greater concentrations ($\log N_w$), and larger shape parameter (μ) values relative to condition 1.

Northwest-to-southwest flow:

(3) Condition 3 is characterized by smaller drop sizes (D_m), larger concentrations ($\log N_w$), and larger shape parameter (μ) values relative to condition 4;
(4) Condition 4 is characterized by larger drop sizes (D_m), smaller concentrations ($\log N_w$), and smaller shape parameter (μ) values relative to condition 3.
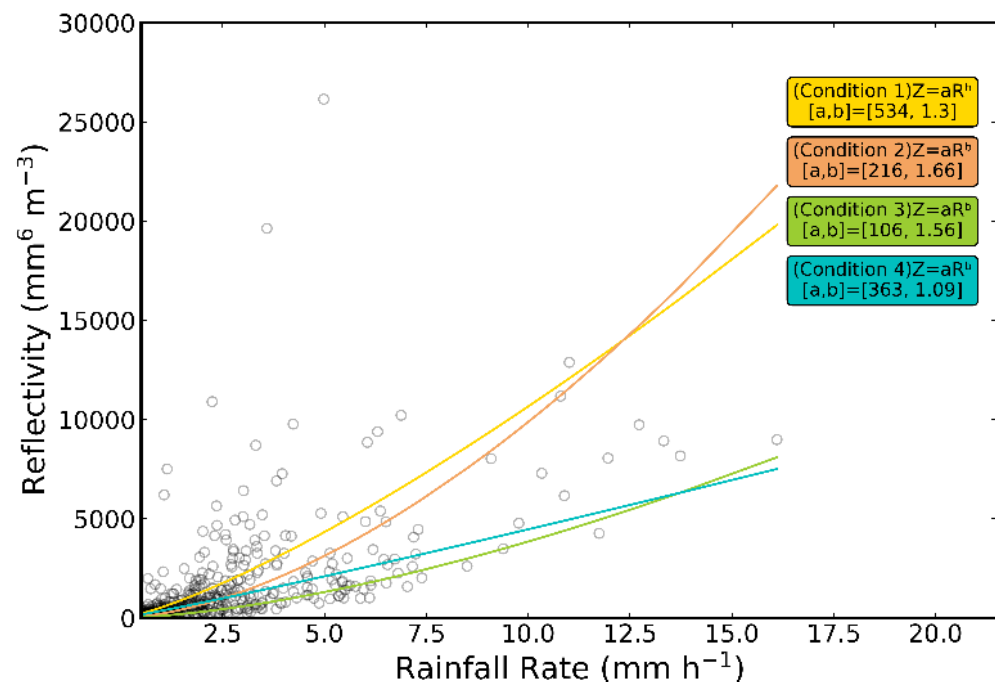

Figure 6. The influence of low-level flow from the northwest and southwest at different magnitudes on the Z–R relationship. The yellow and orange lines represent southeast-to-southwest flow at different magnitudes, while the green and blue lines represent northwest-to-southwest flow at different magnitudes.
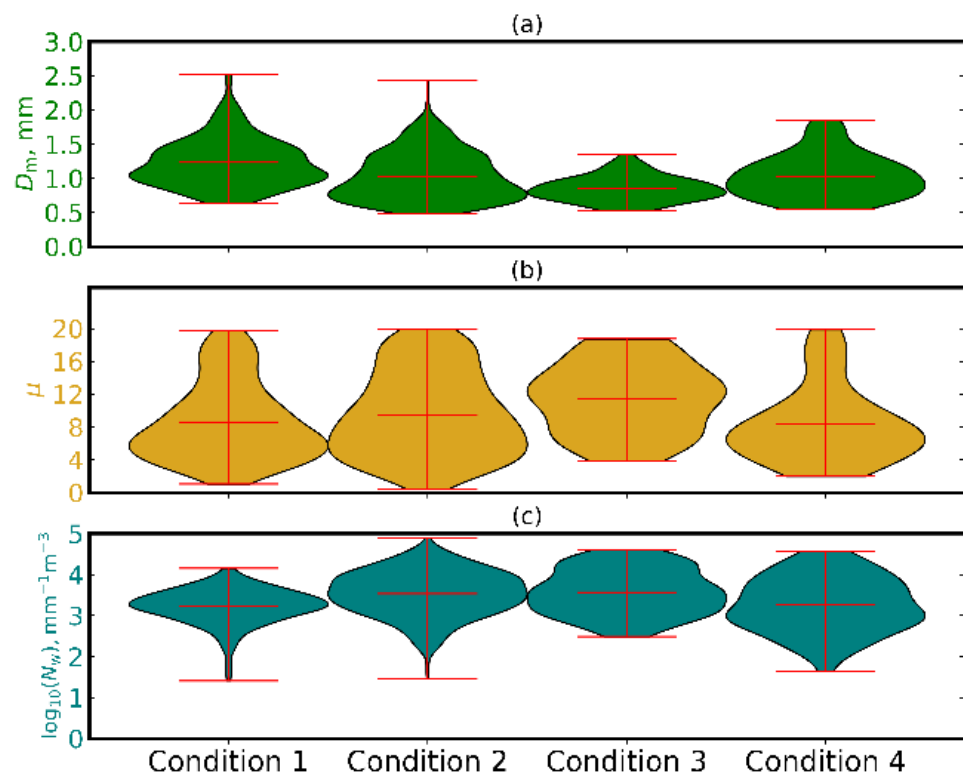
Figure 7. The influence of wind direction and magnitude of low-level flow on the DSD scaling parameters: (**a**) mean mass diameter; (**b**) shape; (**c**) concentration.

Condition 1 is associated with the smallest concentration variability and the largest drop size variability out of all the conditions (Table 8). Figure 8 shows the mode of the normal distribution of the drop size (D_0) for condition 1 (solid black line), favoring larger drop sizes (mostly BB rain) relative to condition 2. The DSD scaling parameter values explains the shift in the Z–R relationship, suggesting greater reflectivity values for low to moderate rain rates. As a result, a larger prefactor (534) and smaller exponent (1.3) are apparent for this condition. Condition 2 is the most interesting of the southwest group, especially regarding the concentration (very high $\log N_w$) and drop size (very low D_m). Figure 8 shows the influence of condition 2 in the form of a normalized distribution of the drop size (D_0), which can be seen in the mode of the distribution for condition 2 (dotted black line) shifted towards smaller drop sizes (mostly NBB). The DSD scaling parameter values explain the shift in the line of best fit in the Z–R relationship, which supports lower reflectivity values for low to moderate rain rates and is associated with a lower prefactor (216) and greater exponent (1.66) relative to condition 1.

Table 8. Statistics that reflect the influence of condition 1 and condition 2 on the DSD parameters. This table includes mean (M), minimum (Min), maximum (Max), and standard deviation (SD).

	Condition 1					**Condition 2**			
	M	**Min**	**Max**	**SD**		**M**	**Min**	**Max**	**SD**
D_0	1.07	0.56	2.41	0.31	**D_0**	0.89	0.41	2.32	0.30
$\log N_w$	3.22	1.41	4.15	0.43	**$\log N_w$**	3.54	1.46	4.88	0.56
D_m	1.23	0.64	2.52	0.35	**D_m**	1.03	0.48	2.43	0.35
μ	8.58	1.04	19.80	4.69	**μ**	9.48	0.44	19.93	5.12

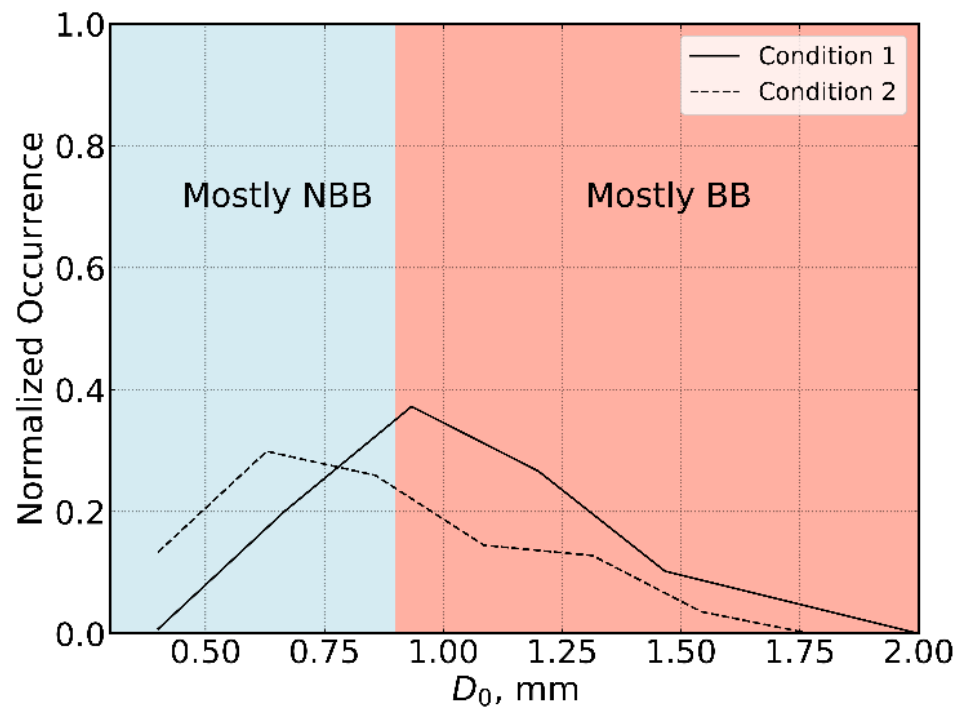**Figure 8.** Normalized distribution of D_0 for condition 1 (black solid line) and condition 2 (black dashed line). Note that smaller drop sizes ($D_0 < 0.90$ mm) are associated with mostly NBB, and larger drop sizes ($D_0 > 0.90$ mm) are associated with mostly BB rain.

Condition 3 represents smaller drop sizes (D_m) and larger concentration ($\log N_w$) values relative to condition 4 and is associated with less variability in size and concentration (Table 9). Furthermore, Figure 9 shows a normalized distribution of the drop size (D_0) for condition 3 (solid black line), which supports smaller drop sizes (mostly NBB). Along with other DSD scaling parameter values, this explains the shift in the Z–R relationship, which supports lower reflectivity values for low to moderate rains rates and is associated with a lower prefactor (106) and larger exponent (1.56) relative to condition 4. Lastly, the normalized distribution of the drop size (D_0) for condition 4 (dashed line) shown in Figure 9 supports larger drop sizes (D_0) relative to condition 3, which is evidenced by the distribution favoring greater occurrences of drops that are larger than 0.90 mm ($D_0 > 0.90$ mm). This is indicative of rain that is mostly BB. Furthermore, larger drop sizes and concentration variability are apparent (see standard deviations in Table 9). The DSD scaling parameter values for this condition explain the shift in the Z–R relationship, which supports greater reflectivity values for low to moderate rain rates and is associated with a greater prefactor (363) and greater exponent (1.09) relative to condition 3.

Table 9. Statistics that reflect the influence of condition 3 and condition 4 on the DSD parameters. This table includes mean (M), minimum (Min), maximum (Max), and standard deviation (SD).

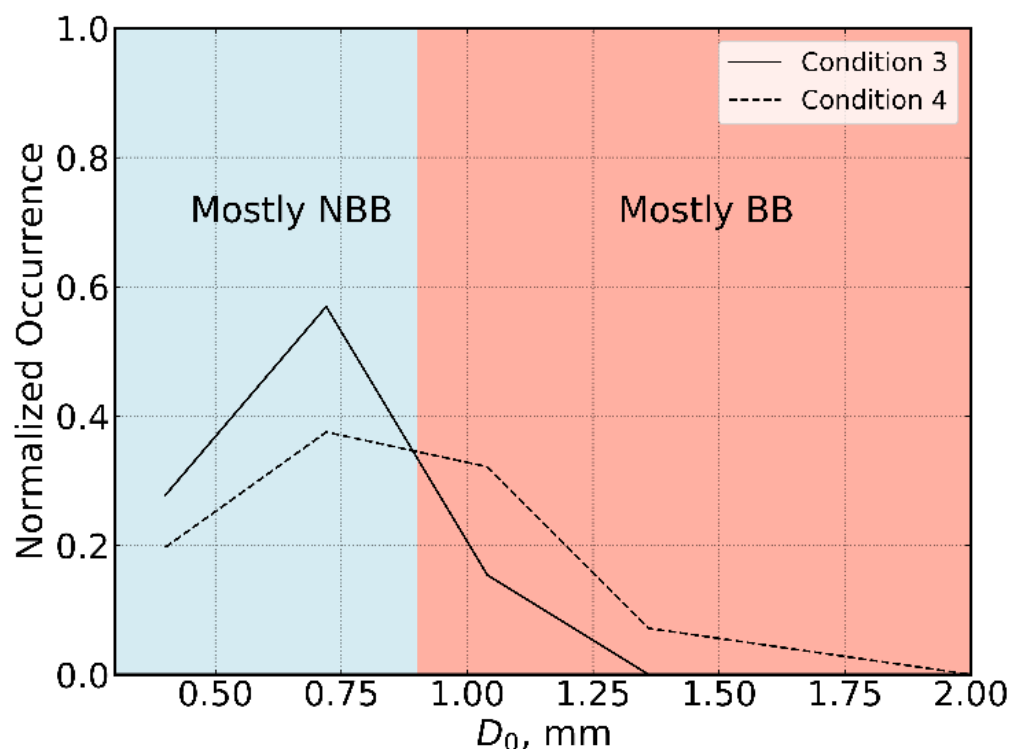|	Condition 3					Condition 4			
	M	**Min**	**Max**	**SD**		**M**	**Min**	**Max**	**SD**
D_0	0.75	0.44	1.19	0.16	D_0	0.89	0.49	1.64	0.27
$\log N_w$	3.56	2.48	4.61	0.53	$\log N_w$	3.26	1.64	4.57	0.66
D_m	0.85	0.52	1.35	0.18	D_m	1.03	0.55	1.84	0.32
μ	11.45	3.82	18.74	4.19	μ	8.32	1.96	19.85	4.55

Figure 9. Normalized distribution of D_0 for condition 3 (black solid line) and condition 4 (black dashed line).

Precipitation characteristics such as median volume diameter (D_0), mean volume diameter (D_m), concentration (N_w), horizontal reflectivity (ZH), and differential reflectivity (Zdr) affect the outcome of the Z–R relationship in Equation (1) (Figure 10). One appreciable feature in Figure 10a,b is the difference in drop sizes(D_0) and concentration ($\log N_w$), with condition 1 showing more occurrences of larger drop sizes and lower concentrations, while condition 2 shows a greater occurrence of smaller drop sizes and greater concentrations. Interestingly, the C-band attenuation correction scheme [28] does not work as well for condition 1 due to the scheme underestimating at smaller reflectivity (ZH) values (see Figure 10e and Table 10). In Figure 10i,j, more occurrences of larger differential reflectivity (Zdr) values are observed in association with drop sizes (D_m) that are greater than 1 mm for condition 1, while more occurrences of smaller differential reflectivity (Zdr) values are observed in association with drop sizes (D_m) of less than 1 mm for condition 2. This suggests that droplets are larger and more oblate under condition 1 (Table 10). Furthermore, more instances of shallow convective rain and fewer instances of heavy stratiform rain coincide with condition 1, which possibly explains the larger drop sizes. Figure 10c,d show the relationship between drop size (D_0) and concentration ($\log N_w$) for northwest-to-southwest flow at different 850 hpa wind magnitudes. Differences are observed under condition 3, as more occurrences of drop sizes (D_0) of less than 1 mm are apparent relative to condition 4. Under both conditions, the C-band attenuation correction scheme [28] shown in Figure 10g,h is accurate between 0 dBZ and 30 dBZ. Additionally, the highest frequencies of horizontal reflectivity (Zh) values occur between 0 dBZ and 15 dBZ for condition 3 and condition 4. Figure 10k,l indicate the relationship between differential reflectivity (Zdr) and drop size (D_m). The most occurrences of differential reflectivity (Zdr) values occur in association with drop sizes (D_m) of less than 1 mm for conditions 3 and condition 4. This suggest that droplets are small and less oblate, on average, for both conditions (Table 11). Additionally, stratiform rain occurs 100 percent of the time under condition 3 and condition 4 (Table 12).
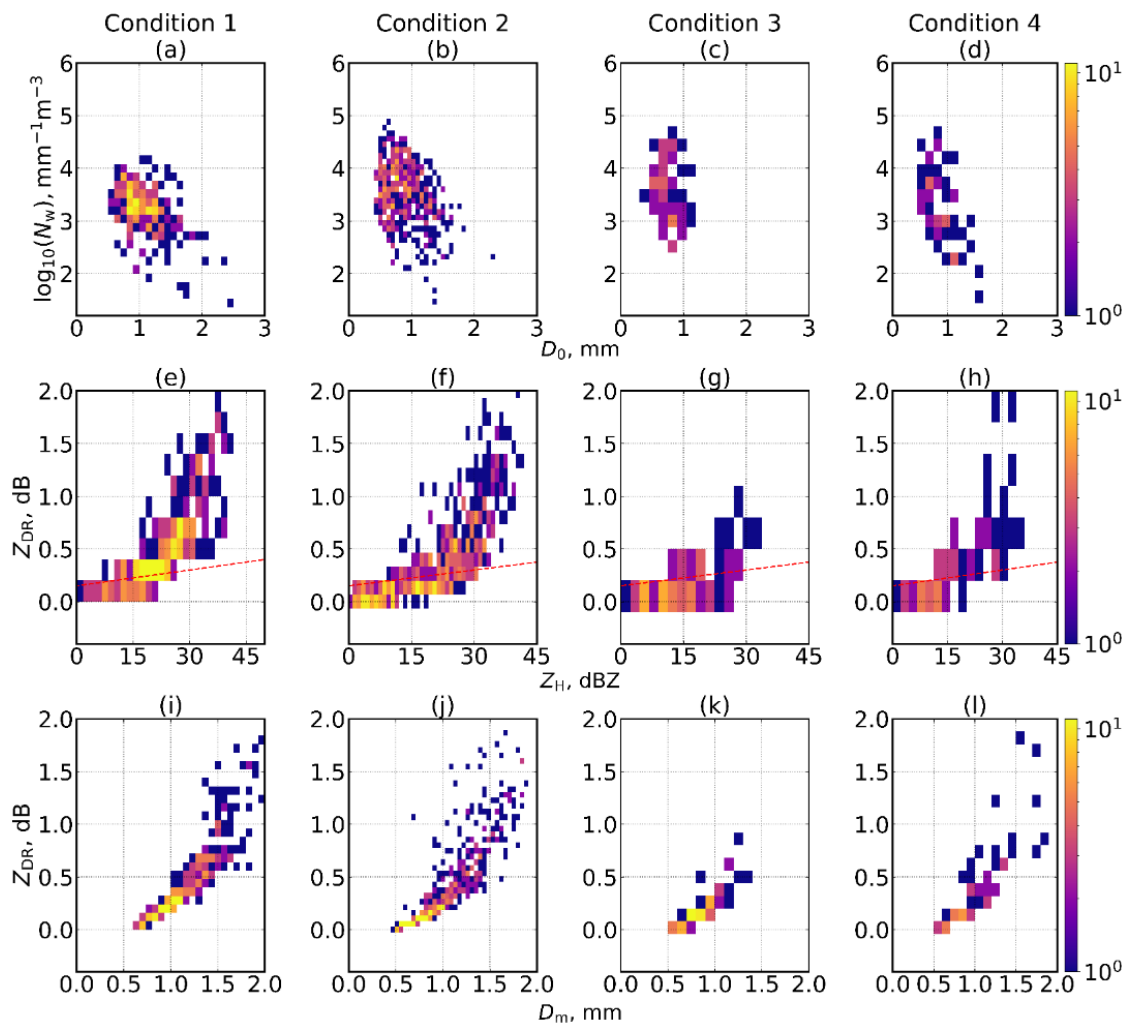
Figure 10. Two-dimensional histograms indicating the influence of wind direction and magnitude on specific DSD and radar parameters: (**a–d**) D_0 vs. $\log N_w$ for condition 1 through condition 4; (**e–h**) ZH vs. Zdr for condition 1 through condition 4; (**i–l**) D_m vs. Zdr for condition 1 through condition 4.

Table 10. Statistics that reflect the influence of condition 1 and condition 2 on the radar parameters. This table includes mean (M), minimum (Min), maximum (Max), and standard deviation (SD).

	Condition 1					Condition 2			
	M	**Min**	**Max**	**SD**		**M**	**Min**	**Max**	**SD**
ZH	22.73	1.66	44.17	8.39	**ZH**	20.5	0.59	42.9	10.35
ZDR	0.54	0.046	2.59	0.43	**ZDR**	0.42	0.013	3.03	0.43

Table 11. Statistics that reflect the influence of condition 3 and condition 4 on the radar parameters. This table includes mean (M), minimum (Min), maximum (Max), and standard deviation (SD).

	Condition 3					Condition 4			
	M	**Min**	**Max**	**SD**		**M**	**Min**	**Max**	**SD**
ZH	15.39	0.71	32.71	7.71	**ZH**	17.51	1.37	35.08	9.08
ZDR	0.20	0.026	0.917	0.17	**ZDR**	0.40	0.029	1.78	0.39

Table 12. Percentage of rainfall type based on 850 hPa wind direction and magnitude. n, number of rainy time steps (5-min); S, stratiform; Heavy S, heavy stratiform; C rain is convective rain; Shallow C, shallow convective.

Condition	n	S (%)	Heavy S (%)	C Rain (%)	Shallow C (%)
1	333	97.3	0.00	0.901	1.801
2	525	97.3	0.381	0.952	1.33
3	63	100	0.00	0.00	0.00
4	56	100	0.00	0.00	0.00

4. Discussion

The San Francisco Bay area is surrounded by complex terrain, which complicates determination of the DSD over time and space. Our analysis showed that regardless of season, stratiform rain dominates this region, accounting for 97 to 100 percent of the rainy time steps for seasonal variation. According to B. Dolan et al. (2018) [29], greater concentrations and smaller drop sizes correspond to vapor deposition, while larger drop sizes and lower concentrations correspond to aggregation/riming and ice-based formation due to thicker clouds. Hence, winter, fall, and spring may be associated with vapor deposition as the dominating microphysical rain-forming process; however, spring may be associated with more occurrences of aggregation/riming and ice-based formation.

Browning et al. (1974) [30] found that the rainfall rate generated by moist feeder clouds is greatest when there is a strong flow of warm, moist air at the lower levels in an orographic environment. Thus, the peculiarities found in southeast-to-southwest flow may have been influenced by an orographic environment, with more instances of weak convection and vapor deposition as the dominating microphysical rain-forming process [29]. Zagrodnik, J.P. et al. (2019) [31]) found that low-level flow in the warm sector of a mid-latitude frontal system aligned with the southwest-facing Quintault valley, WA, resulted in higher raindrop concentrations and enhanced precipitation on the leeward side of the mountain. This was due to strong cross-barrier winds advecting ice particles that originated upstream over complex terrain. Interestingly, condition 2 presented higher concentrations ($logN_w$) and lower drop sizes (D_m and D_0); therefore, it is possible that cross-barrier winds had an impact on the microphysical characteristics under condition 2. Zagrodnik, J.P. et al. (2018) [32] also showed how larger drop sizes and lower concentrations fall into a layer below a deep stratiform cloud layer from the southerly or southeasterly direction and do not have an influence on the Olympic Mountains barrier. This may explain why weak low-level flow coming the southeast to southwest favors a more convective nature and has less orographic influence, as evidenced by larger drop sizes (D_m and D_0) and lower concentrations ($logN_w$).

A comparison of the DSD scaling parameters subjected to different magnitudes of low-level flow from the northwest to southwest indicated smaller drop sizes (D_m and D_0) relative to the southeast-to-southwest flow and produced stratiform rain 100 percent of the time. Zagrodnik, J.P. et al. (2019) [31] found that post-frontal convective showers transition to stratiform characteristics as they traverse from the ocean to more complex terrain. Cannon et al. (2012) [33] found that this phenomenon may be due to the release of a potentially unstable moist layer, causing stratiform precipitation. In contrast, Sikora et al. (2011) [34] found that this phenomenon may correspond to differences in the sensible and latent heat flux between the ocean and land. Since post-frontal systems influencing the San Jose region are associated with northwesterly flow, it is possible that one or a combination of the situations described by Zagrodnik, J.P. et al. (2019), Cannon et al. (2012), and Sikora et al. (2011) [31,33,34] influenced the DSD over San Jose, CA. Differences between stronger and weaker low-level flow from the northwest to southwest produced different results. For instance, condition 4 produced a greater drop size (D_m and D_0) and lower concentration ($logN_w$) relative to condition 3. This may be due to the mixture of convective

and stratiform precipitation, favoring more convective elements on the windward side of the adjacent mountain barriers Zagrodnik, J.P. et al., 2019 [31]. Convective elements may include open-cell cumulus clouds originating in the post-frontal region of a mid-latitude frontal system, which tend to favor forced convection [31,34].

Identifying and distinguishing between different types of rainfall and embedding this information into the Z–R relationship of a single scan is exceedingly difficult—almost impossible. Yielding a fixed prefactor and exponent, such as 'a' of 300 and 'b' of 1.5, results in decent approximations (Hagen et al., 2003, Doelling et al., 1998) [35,36]. Nonetheless, the calculated Z–R relationship is useful for local radar. Figure 11 shows the total Z–R relationship for all recorded data from January of 2019 to April of 2020, along with Z–R relationships built in NEXRAD for comparison.

Figure 11. Observed Z–R relationship. Non-tropical convective $Z = 300R^{1.4}$ ('standard' NEXRAD relation); stratiform/orographic $Z = 200R^{1.6}$ [3]; cool season $Z = 75R^{2.0}$.

5. Conclusions and Future Work

The analysis conducted in San Jose, CA, based on the influence of seasonal variation indicate winter of 2019, fall of 2019, and spring of 2020 showed some influence over the DSD scaling parameters, especially between the winter and spring, characterized by a differentiated Z–R relationship due to larger drop sizes (D_m and D_0) and lower concentrations ($logN_w$) for spring relative to winter. The result is a greater pr-factor (472) and lower exponent (1.37) for spring and a lower prefactor (186) and higher exponent (1.75) for winter. Additionally, the fall Z–R relationship was associated with a prefactor (204) and exponent (1.61) between those of the winter and spring due to DSD scaling parameters falling between those of winter and spring.

Differences in DSD scaling parameters based on directional synoptic flow at the 850 hPa level indicate that most of the rainy time steps occurred in association with southeast-to-southwest flow, which is characterized by a Z–R relationship associated with a higher prefactor (293) and exponent (1.54) relative to the prefactor (188) and exponent (1.4) for northwest-to-southwest flow. This is due to larger drop sizes (D_m and D_0), slightly greater concentrations ($logN_w$), and smaller shape parameter (μ) values.

Direction and magnitude of low-level flow indicate differences in the associated DSD. This study revealed that greater concentration values ($logN_w$), smaller drop sizes (D_m and D_0), and larger shape parameter values (μ) are associated with a stronger low-level flow from the southeast to southwest (condition 2) relative to a weaker low-level flow (condition 1). This explains the smaller prefactor (216) and larger exponent (1.66) associated

with condition 2 relative to condition 1. The DSD associated with strong flow from the northwest to southwest (condition 4) indicates an increase in drop sizes (D_m and D_0), smaller concentration ($\log N_w$) values, and smaller shape parameter (μ) values relative to weaker flow from the northwest to southwest (condition 3). This can be seen in the Z–R relationship under condition 4, which is represented by a larger prefactor (363) and smaller exponent (1.09) relative to condition 3.

Using the rain type scheme proposed in [27] was not sufficient to explain some of the differences in drop size and concentration between the seasons, failing to explain differences in DSD for synoptic events, as most of the rain registered as stratiform. However, adding more disdrometers, in conjunction with the rain types proposed in [27], and differing mesoscale dynamics, such as mountain waves or cross-barrier winds, would be beneficial to form a deeper understanding of DSD in Santa Clara Valley. Based on the reported results, we conclude that the Z–R relationship and the DSD scaling parameters vary by season and direction and magnitude of low-level flow. Therefore, it would be beneficial to use the Z–R relationship to improve rain rate retrieval algorithms.

Author Contributions: Writing—original draft preparation, N.Q.; writing—review and editing, N.Q. and S.C.; supervision, S.C.; project administration and funding acquisition, S.C. All authors have read and agreed to the published version of the manuscript.

References

1. Behringer, D.; Chiao, S. Numerical Investigations of Atmospheric Rivers and the Rain Shadow over the Santa Clara Valley. *Atmosphere* **2019**, *10*, 114. [CrossRef]
2. Shahrban, M.; Walker, J.P.; Wang, Q.J.; Seed, A.; Steinle, P. An evaluation of numerical weather prediction based rainfall forecasts. *Hydrol. Sci. J.* **2016**, *61*, 2704–2717. [CrossRef]
3. Marshall, J.S.; Palmer, W.M. The distribution of raindrops with size. *J. Meteorol.* **1948**, *5*, 165–166. [CrossRef]
4. Ulbrich, C.W. Natural variations in the analytical form of the raindrop size distribution. *J. Clim. Appl. Meteorol.* **1983**, *22*, 1764–1775. [CrossRef]
5. Wu, W.; Zou, H.; Shan, J.; Wu, S. A dynamical z-r relationship for precipitation estimation based on radar echo-top height classification. *Adv. Meteorol.* **2018**, *2018*, 8202031. [CrossRef]
6. Wen, L.; Zhao, K.; Wang, M.; Zhang, G. Seasonal Variations of Observed Raindrop Size Distribution in East China. *Adv. Atmos. Sci.* **2019**, *36*, 346–362. [CrossRef]
7. Hachani, S.; Boudevillain, B.; Delrieu, G.; Bargaoiu, Z. Drop Size Distribution Climatology in CévennesVivarais Region, France. *Atmosphere* **2017**, *8*, 233. [CrossRef]
8. Martner, B.; Yuter, S.; White, A.B.; Matrosov, S.; Kingsmill, D.; Ralph, F. Raindrop Size Distributions and Rain Characteristics in California Coastal Rainfall for Periods with and without a Radar Bright Band. *J. Hydrometeorol.* **2008**, *9*, 408–425. [CrossRef]
9. Siler, N.; Durran, D. What Causes Weak Orographic Rain Shadows? Insights from Case Studies in the Cascades and Idealized Simulations. *J. Atmos. Sci.* **2016**, *73*, 4077–4099. [CrossRef]
10. Mass, C.; Johnson, N.; Warner, M.; Vargas, R. Synoptic Control of Cross-Barrier Precipitation Ratios for the Cascade Mountains. *J. Hydrometeorol.* **2015**, *16*, 1014–1028. [CrossRef]
11. Purnell, D.; Kirshbaum, D. Synoptic Control over Orographic Precipitation Distributions during the Olympics Mountains Experiment (OLYMPEX). *Mon. Weather Rev.* **2018**, *146*, 1023–1044. [CrossRef]

12. Mass, C.; Ferber, G.K. Surface Pressure Perturbations Produced by an Isolated Mesoscale Topographic Barrier. Part I: General Characteristics and Dynamics. *Mon. Weather Rev.* **1990**, *118*, 2579–2596. [CrossRef]

13. Colle, B.A.; Mass, C.F. An Observational and Modeling Study of the Interaction of Low-Level Southwesterly Flow with the Olympic Mountains during COAST IOP 4. *Mon. Weather Rev.* **1996**, *124*, 2152–2175. [CrossRef]

14. Center for Applied Atmopsheric Research and Education. Available online: https://sites.google.com/a/sjsu.edu/caare/resources/facilities (accessed on 16 January 2019).

15. Mocholí Belenguer, F.; Martínez-Millana, A.; Mocholí Salcedo, A.; Milián Sánchez, V.; Josefa Palomo Anaya, M. Disdrometer Performance Optimization for Use in Urban Settings Based on the Parameters that Affect the Measurements. *Symmetry* **2020**, *12*, 303. [CrossRef]

16. Assouline, S. Drop size distributions and kinetic energy rates in variable intensity rainfall. *Water Resour. Res.* **2009**, *45*, W11501. [CrossRef]

17. Wang, Y.; Zheng, J.; Cheng, Z.; Wang, B. Characteristics of Raindrop Size Distribution on the Eastern Slope of the Tibetan Plateau in Summer. *Atmosphere* **2020**, *11*, 562. [CrossRef]

18. Jaffrain, J.; Studzinski, A.; Berne, A. A network of disdrometers to quantify the small-scale variability of the raindrop size distribution. *Water Resour. Res.* **2011**, *47*, W00H06. [CrossRef]

19. Johannsen, L.L.; Zambon, N.; Strauss, P.; Dostal, T.; Neumann, M.; Zumr, D.; Cochrane, T.A.; Blöschl, G.; Klik, A. Comparison of three types of laser optical disdrometers under natural rainfall conditions. *Hydrol. Sci. J.* **2020**, *65*, 524–535. [CrossRef]

20. Testud, J.; Oury, S.; Black, R.A.; Amayenc, P.; Dou, X. The Concept of "Normalized" Distribution to Describe Raindrop Spectra: A Tool for Cloud Physics and Cloud Remote Sensing. *J. Appl. Meteor.* **2001**, *40*, 1118–1140. [CrossRef]

21. Bringi, V.; Chandrasekar, V. *Polarimetric Doppler Weather Radar: Principles and Applications*; Cambridge University Press: Cambridge, UK, 2001; ISBN 9780511541094. [CrossRef]

22. Zhang, G.; Vivekanandan, J.; Brandes, E.; Meneghini, R.; Kozu, T. The Shape–Slope Relation in Observed Gamma Raindrop Size Distributions: Statistical Error or Useful Information? *J. Atmos. Ocean. Technol.* **2003**, *20*, 1106–1119. [CrossRef]

23. Hardin, J.; Guy, N. Zenodo. Available online: https://zenodo.org/record/9991 (accessed on 1 January 2020).

24. Beard, K.; Chuang, C. A New Model for the Equilibrium Shape of Raindrops. *J. Atmos. Sci.* **1987**, *44*, 1509–1524. [CrossRef]

25. NOAA. Operational Model Archive and Distribution System. Available online: https://nomads.ncep.noaa.gov/ (accessed on 1 January 2020).

26. WPC's Surface Analysis Archive. Available online: https://www.wpc.ncep.noaa.gov/archives/web_pages/sfc/sfc_archive_maps.php (accessed on 1 January 2020).

27. Caracciolo, C.; Porcù, F.; Prodi, F. Precipitation Classification at Mid-Latitudes in Terms of Drop Size Distribution Parameters. *Adv. Geosci.* **2008**, *16*, 11–17. [CrossRef]

28. Bringi, V.; Keenan, T.; Chandrasekar, V. Correcting C-band radar reflectivity and differential reflectivity data for rain attenuation: A self-consistent method with constraints. *IEEE Trans. Geosci. Remote Sens.* **2001**, *39*, 1906–1915. [CrossRef]

29. Dolan, B.; Fuchs, B.; Rutledge, S.A.; Barnes, E.A.; Thompson, E.J. Primary Modes of Global Drop Size Distributions. *J. Atmos. Sci.* **2018**, *75*, 1453–1476. [CrossRef]

30. Browning, K.; Hill, F.; Pardoe, C. Structure and mechanism of precipitation and the effect of orography in a wintertime warm sector. *Q. J. R. Meteorol. Soc.* **1974**, *100*, 309–330. [CrossRef]

31. Zagrodnik, J.P.; McMurdie, L.A.; Houze, R.A., Jr.; Tanelli, S. Vertical Structure and Microphysical Characteristics of Frontal Systems Passing over a Three-Dimensional Coastal Mountain Range. *J. Atmos. Sci.* **2019**, *76*, 1521–1546. [CrossRef]

32. Zagrodnik, J.P.; McMurdie, L.A.; Houze, R. Stratiform Precipitation Processes in Cyclones Passing over a Coastal Mountain Range. *J. Atmos. Sci.* **2018**, *75*, 983–1004. [CrossRef]

33. Cannon, D.J.; Kirshbaum, D.J.; Gray, S.L. Under what conditions does embedded convection enhance orographic precipitation? *Q. J. R. Meteorol. Soc.* **2012**, *138*, 391–406. [CrossRef]

34. Sikora, T.D.; Young, G.; Fisher, C.M.; Stepp, M.D. A Synthetic Aperture Radar-Based Climatology of Open-Cell Convection over the Northeast Pacific Ocean. *J. Appl. Meteorol. Climatol.* **2011**, *50*, 594–603. [CrossRef]

35. Hagen, M.; Yuter, S.E. Relations between radar reflectivity, liquid-water content, and rainfall rate during the MAP SOP. *Q. J. R. Meteorol. Soc.* **2003**, *129*, 477–493. [CrossRef]

36. Doelling, I.G.; Joss, J.; Riedl, J. Systematic variations of Z–R-relationships from drop size distributions measured in northern Germany during seven years. *Atmos. Res.* **1998**, *47*, 635–649. [CrossRef]